
Data Invariants to Understand Unsupervised Out-of-Distribution Detection

Lars Doorenbos

Raphael Sznitman

Pablo Márquez-Neila

ARTORG Center for Biomedical Engineering Research
University of Bern
Bern, Switzerland

{lars.doorenbos,raphael.sznitman,pablo.marquez}@unibe.ch

Abstract

Unsupervised out-of-distribution (U-OOD) detection has recently attracted much attention due its importance in mission-critical systems and broader applicability over its supervised counterpart. Despite this increase in attention, U-OOD methods suffer from important shortcomings. By performing a large-scale evaluation on different benchmarks and image modalities, we show in this work that most popular state-of-the-art methods are unable to consistently outperform a simple and relatively unknown anomaly detector based on the Mahalanobis distance (MahaAD). A key reason for the inconsistencies of these methods is the lack of a formal description of U-OOD. Motivated by a simple thought experiment, we propose a characterization of U-OOD based on the invariants of the training dataset. We show how this characterization is unknowingly embodied in the top-scoring MahaAD method, thereby explaining its quality. Furthermore, our approach can be used to interpret predictions of U-OOD detectors and provides insights into good practices for evaluating future U-OOD methods.

1 Introduction

The use of deep learning (DL) models for mission-critical systems, such as in autonomous driving or medicine, is one of the most active research areas in computer vision. Yet, despite impressive performances in recent methods, their ability to extrapolate beyond their training data remains limited. For trained and deployed models, this is particularly problematic when processing images that are corrupted or whose content differs from their expectation. Predictions for unexpected images are often incorrect with high confidence and cannot be identified as such [4]. Ultimately, these silent failures deeply impact the reliability of machine learning systems in mission-critical applications and can have fatal consequences.

To mitigate these limitations, numerous *out-of-distribution* (OOD) detection methods have emerged in the recent past. Closely related to anomaly detection [58] and one-class learning [52], OOD detection aims to spot samples at inference time that do not belong to the training distribution and should not be processed by subsequent machine learning models. At their core, OOD detection methods learn scoring functions that measure the level of anomaly, or *out-of-distributionness*, in test samples with respect to a training data distribution.

Broadly, OOD methods are categorized into supervised and unsupervised, as illustrated in Figure 1. Supervised OOD methods compute an OOD score by using the labels of the training dataset or by knowing the trained downstream network [27, 31, 34]. Conversely, unsupervised OOD (U-OOD) methods are agnostic to the downstream task or data labels, and learn tractable representations of

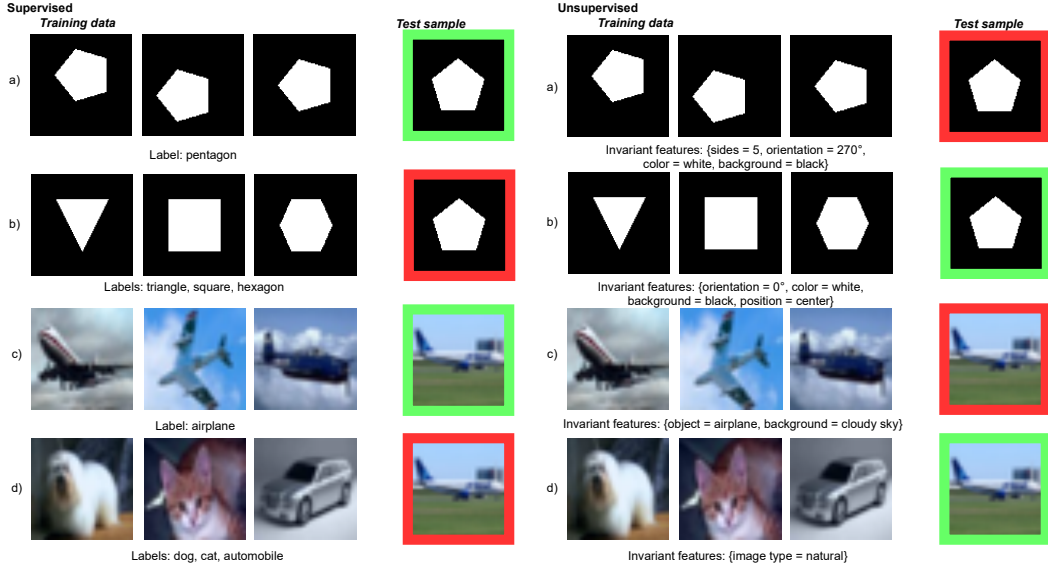


Figure 1: The difference between supervised and unsupervised OOD. For the unsupervised case, invariants in the training data define what should be considered as OOD: in (a) a pentagon at a different angle leads to an OOD test sample, while (b) shows variants in shapes in the training set such that a pentagon is in-distribution at test time. On the other hand, for supervised OOD, this depends solely on the given labels. While the train and test data are the same in each row, the interpretation of OOD differs in the supervised and unsupervised cases. Green and red boxes denote “in” and “out” of distribution samples, respectively. Note that the semantic invariant features listed in the unsupervised cases are used for exemplification purposes, and are not representative of the actual features used in practice.

the training images to compute OOD scores [7, 22, 15, 59], which makes them more general than supervised methods and applicable to a larger range of scenarios.

Considering its significance and generality, the recent emergence of U-OOD methods is unsurprising. Yet with many methods reporting state-of-the-art performance [26, 63, 55, 44, 30, 69, 72, 70, 36], the overwhelming majority of these only validate their approach on one or two tasks. Given the broadness of U-OOD, these limited experimental validations have produced an inconsistent state-of-the-art, while simultaneously establishing an unclear sense of progress in the field. For instance, [28] showed excellent results for one-class tasks using CIFAR10 and ImageNet, only to be contradicted 8 months later in [6] using different data. More alarmingly, this trend of inconsistencies is being perpetuated with evaluation protocols remaining unchanged [30, 42, 5].

For this reason, we first aim to explore and assess the performance and robustness of existing U-OOD detectors by establishing a wide and varied panel of experiments using different datasets and setups. Not only do we show that U-OOD state-of-the-art methods perform erratically when evaluated over a wide and varied range of datasets and tasks (i.e. methods that perform extremely well on some datasets, frequently perform poorly on others), but that the relatively unnoticed MahaAD method [57] consistently outperforms all considered methods by remarkable margins in addition to being extremely simple, stable, and easy to train.

More fundamentally however, we hypothesize that despite the large number of recently proposed U-OOD methods, the main reason for this lack of overall consistency is that the fundamental concept of U-OOD remains vague and ill-defined. In fact, the vast majority of works fail to define U-OOD, let alone provide an intuition to their approach’s functioning. This subsequently leads to brittle methods and weak evaluation protocols.

Intuitively, a test sample should be considered OOD if it *looks different* from training samples. While this intuition seems straightforward, it is unclear how to characterize a training dataset or identify what makes a test sample similar or not to training samples. Yet, characterizing OOD is a fundamental necessity to not only produce reasonable U-OOD detectors, but also to properly evaluate and

understand their behavior. Previous works have overlooked this important step and devised OOD detectors following more or less reasonable heuristics with limited formal justification. For example, using the observation that blurred images are assigned higher likelihoods compared to their original counterparts, SVD-RND [16] leveraged this property to characterize OOD by directly optimizing it. Similarly, [70, 56] identified OOD samples by correcting for their input complexity and the number of background pixels. Other examples include Puzzle-AE [64], which relied on solving puzzles of OOD images worse than their in-distribution counterparts, and MHRot [28] assumed that geometric transformations of OOD samples will be predicted incorrectly.

To this end, we also address here the apparent lack of proper U-OOD definitions by proposing a characterization based on identifying and leveraging image *invariants* of the training set. Following this idea, we formulate the general problem of finding dataset invariants and show that, when constrained to a linear setting, this formulation reduces to the MahaAD method, which unknowingly embodies dataset invariant characterization. Importantly, we show that the invariants found within a training set are more relevant for U-OOD detection than its variant counterparts.

In summary, the contributions of this paper include (1) a thorough evaluation of numerous state-of-the-art U-OOD methods on different tasks and datasets, whereby highlighting that most methods perform erratically and inconsistently, and (2) a novel interpretation of U-OOD using training set invariants, which allows for an appropriate definition of U-OOD. A consequence of the both contributions is that we shed light on why most recent methods do not perform well and, importantly, why MahaAD is an excellent general off-the-shelf U-OOD detector that is consistently superior.

2 Related works

Methods such as one-class support vector machines [68], isolation forest [40], and local outlier factor [12] have traditionally been used for OOD detection in classical machine learning. However these methods suffer greatly when applied to high-dimensional spaces (i.e. images). Unsurprisingly, modern DL based methods have come to replace these more recently. Summarized here are some of the most relevant works on OOD detection using DL, while comprehensive surveys can be found in [13, 49, 58].

In general, U-OOD detection methods rely only on a set of *in*-distribution images to learn the characteristics of the in-distribution data. That is, they do not assume, or have access to, a trained downstream deep network or labeled dataset. Broadly, two families of methods are found in the literature. The first are generative models while the second are based on representation learning.

Generative models: These learn the distribution of images in high-dimensional spaces. However, most generative models are known to perform poorly in OOD detection [15, 46], and many augmentations and improvements have been proposed to increase their performances. [70] showed that the likelihoods obtained by models such as Glow [35] or PixelCNN++ [65] are heavily influenced by the input complexity, and propose a likelihood ratio to correct for this. Interestingly, the work in [56] showed that background pixels dominate test sample likelihood scores, and attempt to correct for these by using the likelihood of a second model that tries to capture the population level background information. Similarly, Schirrmeister *et al.* [66] use the likelihood ratio with respect to a second model trained on a general, large scale dataset.

Representation learning: Instead of working in the image space, most U-OOD methods aim to learn a low-dimensional image embedding. Here, many works have opted for self-supervised learning strategies to simulate classification problems and train DL models to representative image features. One popular approach is predicting geometric transformations, such as image rotations, translations, scales, flips, or patch re-arrangements [7, 22, 28, 77]. Other self-supervised approaches rely on auto-encoders and optionally perturb the input in some way to create more robust feature descriptions. Example perturbations include adding noise [61] or shuffling patches [64]. Further extensions propose to fit an auto-regressive model to the latent space [1] or to add a memory module [23].

Bergman *et al.* [6] find that scoring samples by the distance to their *k*-nearest neighbours (kNN) in the space of pre-trained ImageNet features outperformed self-supervised methods. Xiao *et al.* [79] showed that features obtained from self-supervised—rather than supervised—training on ImageNet pushed performance even further. Most recently, approaches based on contrastive learning [69, 72], or focused on adapting pretrained features [54, 55], have been advantageous. Finally, Rippel *et*

al. [57] combined Mahalanobis distances in the space of ImageNet features to beat the previous state-of-the-art on the MVTEC dataset.

3 Invariants for Unsupervised OOD

In the supervised setting, similar to the problem of zero-shot learning, a sample is considered OOD if it cannot be assigned to one of the training set classes. In the unsupervised setting, however, defining OOD is more challenging as we do not know *a-priori* what and if any classes are present at all. As done in anomaly detection [58], one potential approach to define U-OD could be to measure if a sample lies in a low-density region of the training data. But doing so would be short-sighted because whether few or many image examples of a specific class appear in a training set may only be a reflection of their natural prevalence, rather than being a real OOD sample. For instance, if one had a training set of dogs, the Norwegian Lundehund (i.e. a rare dog breed) would most likely appear in low-density regions of the training distribution, in contrast to German Shepherds (i.e. very common breed). Yet both should still be considered dogs. Instead, we propose to use *invariants* as a way to characterize U-OD. Specifically, our idea is to first determine image invariants in the training set, and then detect OOD test samples by identifying if they keep the invariants of the training set.

To illustrate this, consider the toy examples in Fig. 1, where four different combinations of training sets and test examples are given. Recall that for the unsupervised case, no labels in the training data are available thus losing context as to what is or is not semantically OOD. However, the necessity to leverage context to disentangle relevant and irrelevant aspects of images remains key for U-OD detection, since it is too broad to be meaningful without it (as stated in [2]). Hence, we assume that this necessary context is provided by a set of general features that we have at our disposal, that can describe the input images \mathbf{x} . For instance, these features could be $\mathbf{f}(\mathbf{x}) = \{\text{sides}(\mathbf{x}), \text{orientation}(\mathbf{x}), \text{color}(\mathbf{x}), \dots\}$, or features coming from a network pre-trained on a general dataset. Given this, we want to summarize a training set by the *union* of features that are invariant over the entire training set. For example, Fig. 1(a) would use the combination of invariant features $\{\text{sides} = 5, \text{orientation} = 270^\circ, \text{color} = \text{white}, \text{background} = \text{black}\}$, and similarly $\{\text{orientation} = 0^\circ, \text{color} = \text{white}, \text{background} = \text{black}, \text{position} = \text{center}\}$ for Fig. 1(b). At inference time then, a test sample described by this union of invariant features would be OOD if these features are no longer invariant with respect to the training set. In this sense, variant features from a dataset are in fact irrelevant for U-OD detection, which stands in contrast to many previous methods that focused on learning a representation of the training distribution (e.g., [16, 41, 84]).

In the remainder of this section, we begin by formalizing the above-mentioned idea and propose an approach to identifying these invariants for the general case. We then show how this is related to the MahaAD method [66]. In the experimental section, we demonstrate how MahaAD performs in comparison to recent methods and how it behaves in light of image invariants.

3.1 Formalization

Given a training set $\{\mathbf{x}_i\}_{i=1}^N$, with corresponding feature vectors, $\mathbf{f}(\mathbf{x}_i) \equiv \mathbf{f}_i \in \mathcal{F}$, we define an invariant as a non-constant function $g : \mathcal{F} \rightarrow \mathbb{R}$, such that $g(\mathbf{f}_i) = 0, \forall i$. That is, g is an invariant if it computes a constant value (i.e., $g(\mathbf{f}_i) = 0$) for the elements of the training set, but in general may not compute the same constant value for other elements (e.g., elements of a test set). Our goal then is to find a set of invariants, $G = \{g_1, \dots, g_K\}$, over the set of training feature vectors. While doing so in one global optimization is challenging, we propose to solve this by solving a sequence of K problems, one per invariant,

$$\begin{aligned} g_k(\mathbf{f}_i) &= 0 \quad \forall i, \\ \|\nabla g_k(\mathbf{f}_i)\|_2 &\neq 0 \quad \forall i, \\ \nabla g_k(\mathbf{f}_i) \cdot \nabla g_j(\mathbf{f}_i) &= 0 \quad \forall i, j < k, \end{aligned} \tag{1}$$

where the first equality makes g_k zero for all training samples, the second equality prevents g_k from becoming a projection (i.e., effectively making it non-constant) and the third equality requires that new invariants are different from all previously found invariants by making their gradients mutually orthogonal. After finding G , a test feature vector \mathbf{f} will be considered OOD if $g_k(\mathbf{f}) \neq 0$ for any invariant k .

As noisy real-world data rarely lies in an exact manifold, solving Eq. (1) is unfeasible in practice even for a small number of invariants K . Instead, we relax Eq. (1) and express it as a minimization problem to find a set of soft invariants,

$$\begin{aligned} \min_{g_k} \frac{1}{N} \sum_i g_k(\mathbf{f}_i)^2, \\ \text{s.t. } \|\nabla g_k(\mathbf{f}_i)\|_2 = 1 \quad \forall i, \\ \nabla g_k(\mathbf{f}_i) \cdot \nabla g_j(\mathbf{f}_i) = 0 \quad \forall i, j < k, \end{aligned} \quad (2)$$

where we constrain the magnitude of the gradient to 1 to prevent g_k from arbitrarily compressing its output and minimizing the loss artificially.

Once $G = \{g_1, \dots, g_K\}$ is established, any test vector \mathbf{f} can be scored by computing the ratios between the test error and the average training error,

$$s^2(\mathbf{f}) = \sum_k \frac{g_k(\mathbf{f})^2}{e_k}, \quad (3)$$

where e_k is the training MSE of the soft invariant g_k ,

$$e_k = \frac{1}{N} \sum_i g_k(\mathbf{f}_i)^2. \quad (4)$$

Intuitively, tight invariants with low e_k values will have a high influence in the final score, while weak invariants with large e_k values will essentially be ignored. Given that the contribution of weak invariants is negligible in s^2 , we can circumvent the problem of setting an optimal number of invariants K and safely set K to the dimensionality of the feature space.

We can further simplify the optimization problem of Eq. (2) by constraining the invariants to the family of affine functions $g_k(\mathbf{f}) = \mathbf{a}_k^T \mathbf{f} + b_k$ with unitary \mathbf{a}_k . Under these conditions, Eq. (2) reduces to a PCA problem. Its solution sets \mathbf{a}_k to the k -th smallest principal component and the squared error e_k is set to its corresponding eigenvalue. Moreover, the score function Eq. (3) can be re-written as the square of the Mahalanobis distance using the mean and the covariance of the training feature vectors. Ultimately, computing Mahalanobis distances properly weighs and exploits the linear invariants in the training dataset, which, in turn, suggests that the Mahalanobis distance could lead to good OOD detectors despite its simplicity.

3.2 The Mahalanobis anomaly detector

Given the above, we briefly revisit the the Mahalanobis anomaly detector (MahaAD) from Rippel *et al.* [57] as it embodies the invariant feature learning we propose. Fig. 2 illustrates the approach.

MahaAD uses the spatial pooling of the feature maps of a pre-trained CNN to define feature descriptors \mathbf{f} . Instead of choosing a specific CNN layer for \mathbf{f} , MahaAD works in a multi-layered manner describing each input image \mathbf{x} with a collection of feature vectors $\{\mathbf{f}_\ell(\mathbf{x})\}_{\ell=1}^L$ computed at L different layers.

At training time, MahaAD computes the mean and the covariance of the descriptor vectors of the images in the training dataset $\{\mathbf{x}_i\}_{i=1}^N$. Specifically, for each layer ℓ , the mean is computed as,

$$\boldsymbol{\mu}_\ell = \frac{1}{N} \sum_{i=1}^N \mathbf{f}_\ell(\mathbf{x}_i), \quad (5)$$

while the corresponding covariance matrix is,

$$\boldsymbol{\Sigma}_\ell = \frac{1}{N} \sum_{i=1}^N (\mathbf{f}_\ell(\mathbf{x}_i) - \boldsymbol{\mu}_\ell)(\mathbf{f}_\ell(\mathbf{x}_i) - \boldsymbol{\mu}_\ell)^\top. \quad (6)$$

To avoid singular covariance matrices in high-dimensional or low-data regimes, shrinkage is applied in practice by adding a small multiple of the $d \times d$ identity matrix to each $\boldsymbol{\Sigma}_\ell$. By using multi-layer feature vectors, MahaAD is able to find linear invariants at different image scales.

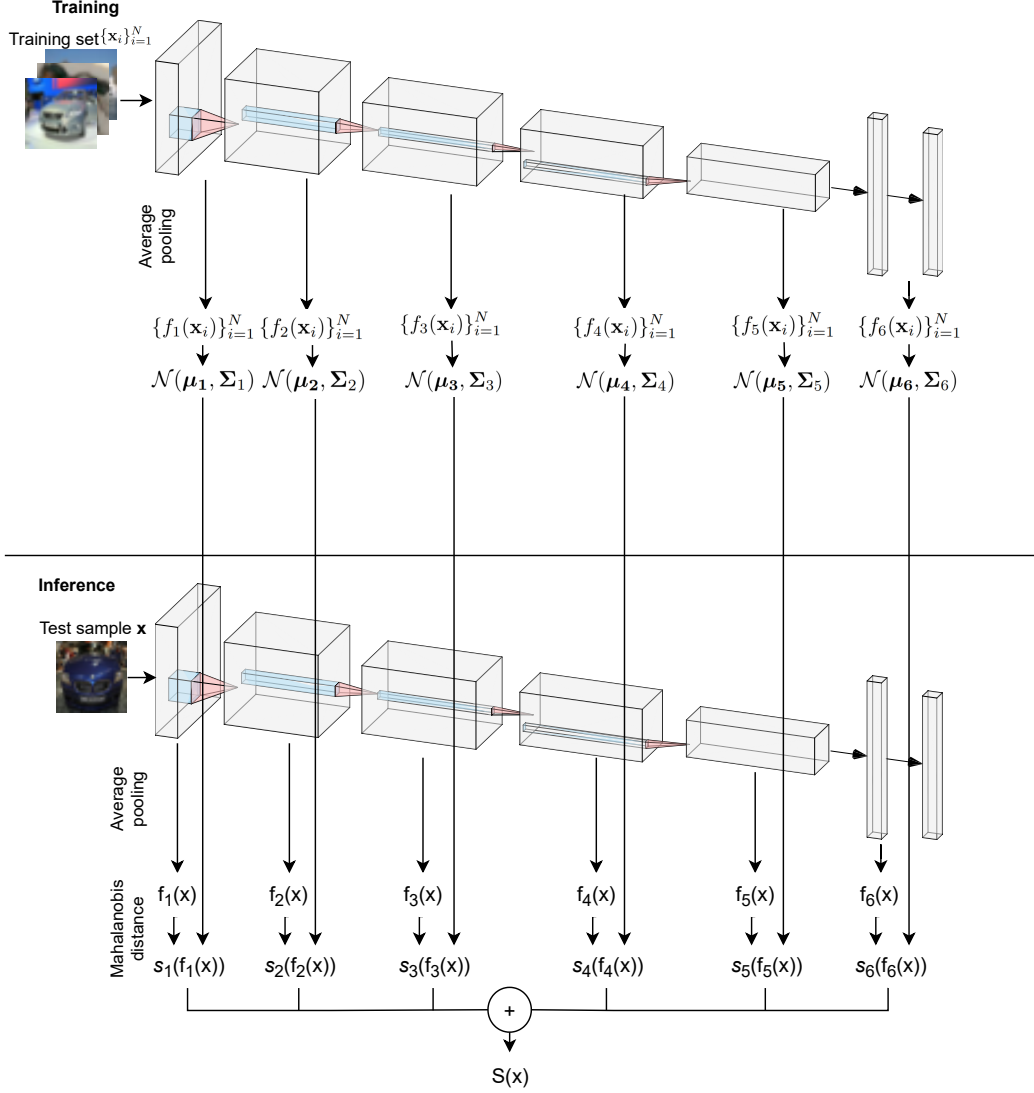


Figure 2: Training and inference stages of the MahaAD method.

Importantly, the CNN from which the features are computed is not trained or tuned to the training set whereby making this training phase simple and extremely fast. In practice, it makes the approach more stable and robust across a larger number of datasets. This differs from most recent U-OOD methods that opt to fine-tune their DL models to the training set [55, 69, 72].

At test time, MahaAD computes the layer-wise Mahalanobis distances between the descriptor vectors of the test image x and the means $\{\mu_\ell\}_\ell$,

$$s_\ell(\mathbf{f}) = \sqrt{(\mathbf{f} - \mu_\ell)^\top \Sigma_\ell^{-1} (\mathbf{f} - \mu_\ell)}, \quad (7)$$

which is equivalent to the square root of Eq. (3). The final OOD score is the sum of the scores over all layers,

$$S(\mathbf{x}) = \sum_{\ell=1}^L s_\ell(\mathbf{f}_\ell(\mathbf{x})). \quad (8)$$

4 Experiments

To explore the current state of U-OOD detection, we compare the performance of several state-of-the-art U-OOD methods over a collection of 76 experiments that involve different image modalities, sizes, perturbations, and different criteria for the in- and out-distributions. These experiments aim to identify in what scenarios different methods may be effective and which may not be. As such, we group our experiments into six categories outlined below and illustrate some of them in Fig. 3:

Unimodal class (*uni-class*). Similar to most works[54, 69, 72, 63, 30, 36, 28], we perform 10 experiments using the CIFAR10 dataset, where each experiment takes one of the 10 classes as in-distribution and uses the remaining 9 as OOD.

Unimodal superclass (*uni-super*). Comparable to *uni-class* using CIFAR100, we perform 20 experiments, where each of the 20 semantic superclasses of CIFAR100 are used as in-distribution and treat all remaining 19 superclasses as OOD [6, 72, 22, 54].

Unimodal anomaly (*uni-ano*). We use the MVTEc dataset [9] which contains 15 classes of images of perfect and defect objects (each class has between 60 and 391 training samples). As in [57, 19, 38, 54, 71], we perform one experiment per class, where the defect-free images are used for the in-distribution training set and test images are the defect-free OOD samples.

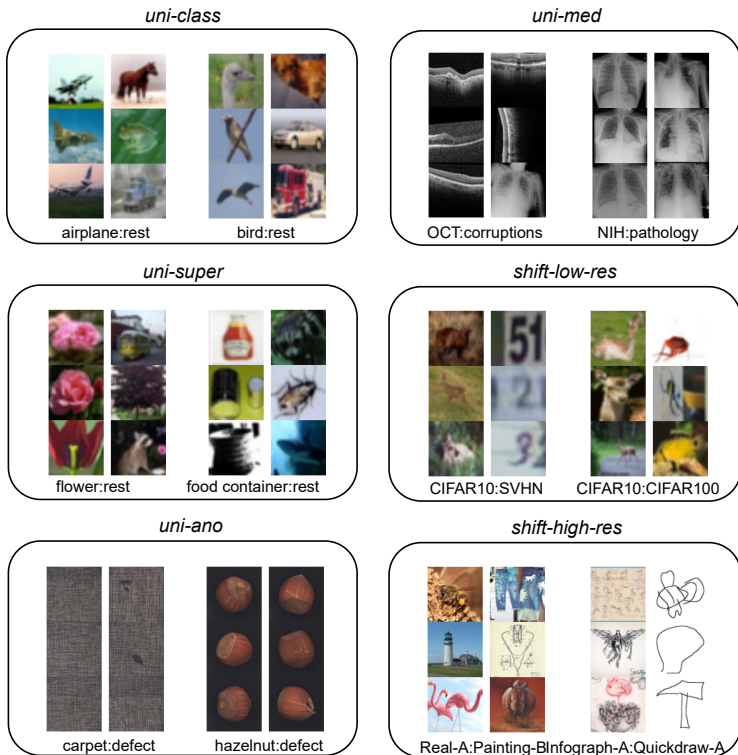


Figure 3: Example in-distribution and OOD images for each task considered.

Unimodal anomaly medical (*uni-med*). We perform 7 experiments with different medical image modalities. The first 2 experiments use optical coherence tomography (OCT) scans and chest X-rays as training in-distributions and corrupted images as OOD samples. The 3rd experiment trains the models with healthy chest X-rays and uses pathological chest X-rays as OOD. In the remaining 4 experiments, healthy retinal fundus photographs are used for the in-distribution and pathological fundus photographs of four increasing severity levels are used for the OOD images [48, 41, 11, 73].

Low-resolution domain shift (*shift-low-res*). 2 experiments that share CIFAR10 as the in-distribution and use SVHN and CIFAR100 as OOD [69, 72, 44, 70, 43].

Method	Architecture	<i>uni-class</i>	<i>uni-super</i>	<i>uni-ano</i>	<i>uni-med</i>	<i>shift-low-res</i>	<i>shift-high-res</i>		Category mean	Experiment mean
							Real-A	Infograph-A		
MSCL	ResNet-152	97.5 ± 0.1*	96.5*	87.2*	71.6 ± 0.2	81.0 ± 0.0	79.5 ± 0.1	71.0 ± 0.0	83.5	85.9
DN2	ResNet-152	92.5*	90.5	88.0	<u>76.0</u>	76.9	68.9	75.2	81.1	83.2
SSD₃₂	ResNet-101	90.0*	80.4 ± 0.3	65.8 ± 3.0	64.6 ± 0.6	95.1*	61.6 ± 0.5	57.3 ± 1.3	73.5	71.6
SSD₂₂₄	ResNet-50	-	-	63.5 ± 1.4	63.4 ± 3.4	-	53.8 ± 1.7	45.5 ± 6.4	-	-
MKD	VGG-16	87.2*	89.9 ± 0.1	87.7*	74.7 ± 0.2	44.5 ± 1.8	48.9 ± 0.3	83.0 ± 0.4	73.7	79.6
DDV	ResNet-50	59.8 ± 0.4	60.4 ± 0.7	70.5 ± 0.6	66.8 ± 2.7	56.0 ± 3.3	63.5 ± 1.7	61.0 ± 2.6	62.6	63.3
MHRot	ResNet-101	90.1*	80.1 ⁺	70.8 ± 1.0	69.0 ± 0.7	<u>90.1⁻</u>	59.7 ± 1.5	<u>86.7 ± 0.2</u>	78.1	76.8
Glow	K = 32, L = 3	53.7 ± 0.0	53.8 ± 0.1	82.0 ± 2.5	55.8 ± 0.8	30.3 [†]	36.9 ± 0.0	34.4 ± 0.1	49.6	53.7
IC	K = 32, L = 3	55.3 ± 0.0	55.9 ± 0.1	73.6 ± 2.6	65.1 ± 0.5	66.4 [†]	68.0 ± 0.0	61.3 ± 0.1	63.7	63.0
HierAD	K = 32, L = 3	64.2 ± 0.0	62.4 ± 0.6	81.6 ± 2.1	72.5 ± 0.6	80.4*	61.8 ± 0.3	84.1 ± 0.2	72.4	70.9
MahaAD	ResNet-101	92.6	92.3	91.3	74.9	84.2	69.8	83.8	84.1	85.8
MahaAD	ResNet-152	93.1	92.6	91.8	75.3	86.6	70.4	83.7	84.8	86.3
MahaAD	EfficientNet-b4	<u>96.0</u>	<u>94.6</u>	94.4	76.8	87.7	<u>74.9</u>	88.5	87.6	89.2

Table 1: Performance summary: AUC mean and standard deviation (over three runs) for evaluated methods. We report performances for each category, as well as the mean over categories and over experiments. No standard deviation is reported for **MahaAD** and **DN2** as they are deterministic. A more detailed breakdown can be found in the supplementary material. (*) Taken from original publication; (+) taken from [54]; (-) taken from [72]; (†) taken from [66].

High-resolution domain shift (*shift-high-res*). An extended version of the experiments on the dataset DomainNet presented by Hsu et al. [31]. We run 22 experiments separated into two groups: 11 experiments with Real-A as the in-distribution and 11 experiments with Infograph-A as the in-distribution, using in both cases each of the remaining 11 modalities as OOD.

When referring to a specific experiment, we will use the notation in-dataset:out-dataset.

Evaluated methods: We evaluate a selection of the top-performing U-OOD detection methods, which we selected if they were among the top-performing methods in at least one of the above tasks. These include: **MSCL** [54], **DN2** [6], **SSD** [69], **MHRot** [28], **MKD** [63], **DDV** [41], **Glow** [35], **IC** [70] and **HierAD**[66].

All methods are used with their default hyperparameters as given in their official implementations, with the architecture selected as large as possible under those settings and given memory restrictions. More details can be found in the supplementary material. No hyperparameter search was performed, given that no validation metric exists. Specifically, for **MKD** we use a VGG-16, as all its default settings were selected with it in mind. **Glow**, **HierAD** and **IC** models are based on the same Glow network. **MSCL** and **DN2** use a ResNet-152, **SSD₃₂** and **MHRot** a ResNet-101 and **SSD₂₂₄** and **DDV** a ResNet-50. As prior work found the ResNet size does not have a large effect on OOD detection performance for self-supervised methods [54, 69], we prioritize a larger batch size over larger architectures, given memory restrictions. All methods resize the input images to 224×224 , with the exception of the Glow-based and **SSD₃₂** models, that resize images to 32×32 .

For fair comparison, we show results when using **MahaAD** with a ResNet-101, ResNet-152 and an EfficientNet-b4. Note that using a pre-trained CNN to extract image features is not a major limitation in practice, as all standard deep learning libraries offer tools to load and use such models in very few steps. Also, we show in our results that the typical ImageNet-based features extrapolate well to other very different image modalities (i.e. *uni-med*).

4.1 Results

The evaluated methods were compared in terms of performance, training times and training complexity. We detail the results of our experiments below and provide a deeper breakdown of the results, including additional methods, in the supplementary material.

Performance. Most methods were inconsistent across different tasks (see Table 1). **MSCL**, which performed very well in *uni-class* and *uni-super*, is challenged in *uni-med* and in *shift-high-res* with Infograph-A as in-distribution. Conversely, **MKD**'s performance is high for *uni-med*, but heavily drops in *shift-low-res*. **SSD** had the best results on *shift-low-res* but struggled with tasks involving

high-dimensional images, and **DN2** scored very well on average except on tasks involving domain shift. On the other hand, **MahaAD** performed very well and with high stability across tasks. Specifically, it performed best or second-best in all tasks but in the low resolution domain shift tasks, while still beating **MSCL**, **DN2**, **MKD** and **DDV** by large margins. Furthermore, **MahaAD** was the best performing method on average, beating the second-best method, **MSCL**, by more than 4 percent points. In addition, we observed this for different network architectures. In all following experiments, we fixed the architecture of **MahaAD** to EfficientNet-b4, unless stated otherwise.

These performance instabilities were not only observed across the different tasks reported in Table 1, but also within the tasks with fixed in-distribution across different OOD datasets. For example, for the *shift-high-res* category, performance of most methods fluctuated depending on the chosen OOD dataset (see Fig. 4). In contrast, **MahaAD** again is the only method that stands out in terms of stability, as it performs well regardless of the in and the out datasets selected.

Training times. **MahaAD** was faster to train than its counterparts (see Fig. 5). For example, in the CIFAR10:SVHN experiment (task *shift-low-res*), using two GeForce RTX 3090, **MahaAD** was the fastest to train, taking roughly 90 seconds to process the entire CIFAR10 dataset. Other methods with similar performances were orders of magnitude slower: **MSCL** took more than half an hour for airplane:rest and **SSD** took more than 12 hours for CIFAR10:SVHN. In addition, no method performed consistently better than **MahaAD** on either of these two experiments. This behavior was also observed for the rest of experiments.

Training complexity. Furthermore, **MahaAD** was simpler to train, with fewer hyperparameters and more predictable behavior. Predicting the convergence of methods such as **MSCL** and **DDV** was challenging as there is no apparent correlation between the training loss and OOD performance, as also reported in [54]. It is thus unclear when to stop training before the performance starts

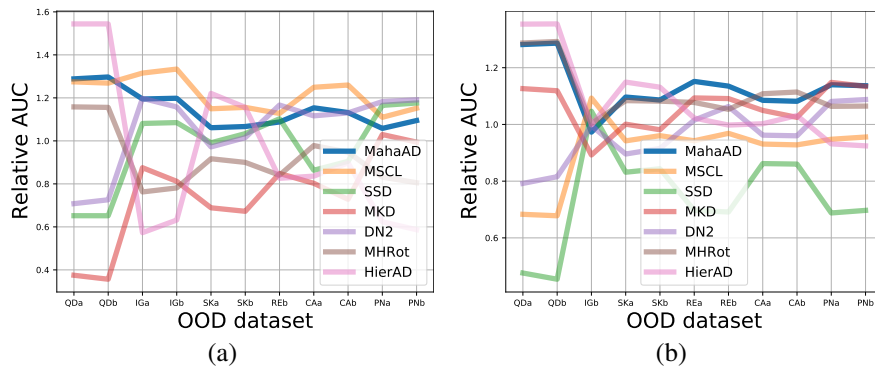


Figure 4: Relative performance (AUC divided by mean AUC on that task) for seven methods on the *shift-high-res* tasks. X-axis indicates the out distribution. (a) Real-A as in-distribution. (b) Infograph-A as in-distribution.

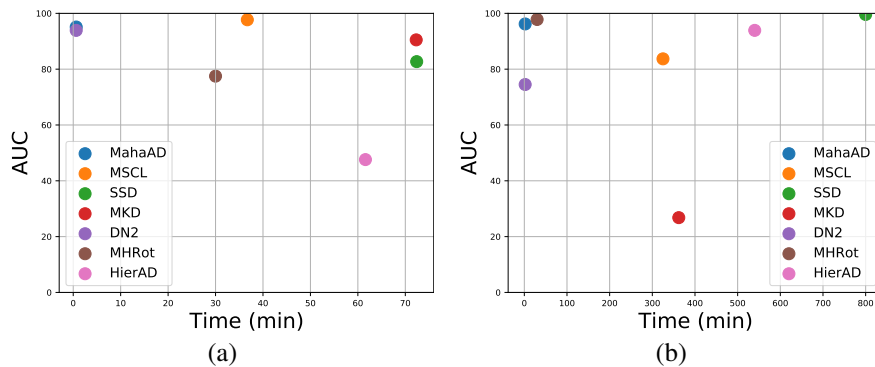


Figure 5: Training times and performances for different methods on (a) *uni-class's* airplane:rest and (b) *shift-low-res's* CIFAR10:SVHN.

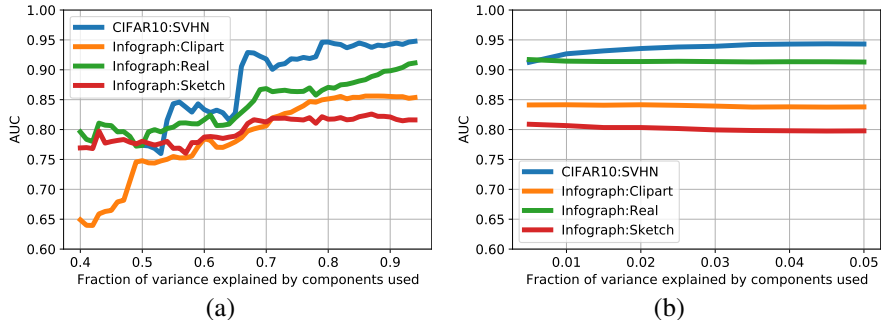


Figure 6: The OOD AUC for four experiments with a ResNet50 using different sets of principal components. (a) gives result starting for the first principal components, while (b) does so from the last principal components. For example, using the most variant components, which together explain 50% of the variance per layer, gives an AUC score for CIFAR10:SVHN of around 77%, whereas using the least variant components responsible for just 1% of the variance results in an AUC of around 93%. The x-axis of (a) starts at 0.4 as for Infograph the most variant component of the first layer is responsible for almost 40% of all variance. For CIFAR10, this is close to 50%.

degrading. While this lack of obvious stopping criterion is problematic for many methods [55, 54, 59, 51], **MahaAD** is convenient as it avoids this necessity altogether.

4.2 Importance of data invariants

We report here additional results that support the importance of data invariants, both for the quality of U-OOD detection and as a tool to analyse U-OOD predictions and evaluation datasets.

In order to assess the importance of data invariants for U-OOD detection, we examined which principal components are most effective at identifying OOD samples. To that end, we measured the AUC score in four experiments by limiting the Mahalanobis score of Eq. (3) to only use subsets of principal components with highest variance, corresponding to the modes of variation of data. Similarly, we observed the performance with subsets of principal components with smallest variance, corresponding to data invariants. The latter outperformed the former by a large margin in U-OOD detection (see Fig. 6). Starting from the most variant principal components, the performance slowly increases when adding more components, converging when over 80% of the variance is explained. On the other hand, when starting from the most invariant component, the performance quickly converges when as little as 3% of the variance has been explained, supporting the idea that invariants are more representative to characterize training data and OOD samples. While other works had observed similar findings, they either consider the supervised case [34, 53], or frame it in the context of reducing dimensionality [57].

An interesting consequence of our invariant-based interpretation of U-OOD is that some experiments that are valid for evaluating supervised OOD methods, are in fact not suitable for the U-OOD case. For instance, CIFAR10:CIFAR100 [44, 69, 43] or 9-classes:1-held-out-class of CIFAR10 [3, 6] were used in previous U-OOD works even though they do not appear to meet the U-OOD criteria.

More specifically, according to our definition for U-OOD, one would expect that by increasing the number of classes present in a training set, the invariants associated to the high semantic features will decrease, effectively reducing the probability that new classes are considered U-OOD. For example, training with multiple classes from CIFAR10 (e.g., cats, dogs, cars) reduces the probability that an additional class (e.g., plane) from CIFAR10 or CIFAR100 should be considered OOD (Fig. 1(d)). Following our invariant formulation however, the number of training classes should not affect the probability that images from a different modality are detected as OOD, as they break other kind of invariants. For instance, when training with images from CIFAR10, the test images from SVHN or MNIST should still be considered OOD regardless of the number of CIFAR10 training classes, as they are clearly distinct in appearance.

In Fig. 7, we investigate this desired behavior experimentally by analyzing the performance of the three best-performing methods when we increased the number of in-distribution CIFAR10 training classes. As expected, all methods consider fewer images from CIFAR100 and one held-out class

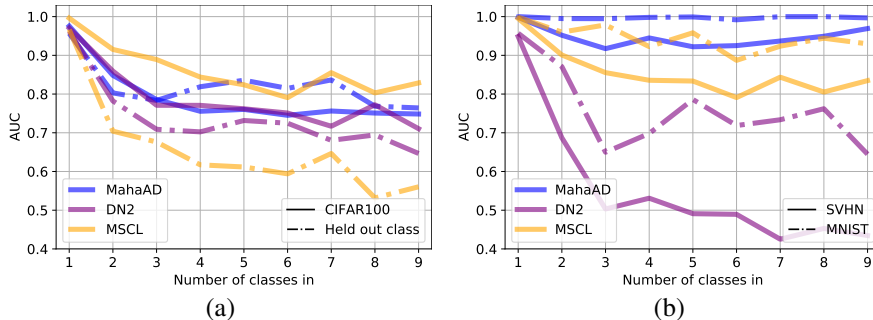


Figure 7: OOD AUC performance for different methods as a function of the number of classes in the training set (CIFAR10), keeping its size constant. (a) Performance on CIFAR100 (full line) and a held out CIFAR10 class as out-distribution (dashed line), which should not be considered U-OOD under our interpretation. (b) Performance on SVHN (full line) and a held out MNIST class as out-distribution (dashed line), which should be considered U-OOD under our interpretation.

from CIFAR10 as OOD when the number of training classes increased (Fig. 7(a)). Conversely, increasing the number of training CIFAR10 classes did not affect the predictions for SVHN and MNIST with **MahaAD**, which correctly kept detecting both datasets as OOD (Fig. 7(b)). In contrast, this did negatively affect the predictions of **DN2** and **MSCL**. According to our invariant-based interpretation of U-OOD, **MahaAD**'s behavior is reasonable and consistent in these configurations, yet the unexpected **DN2** and **MSCL** results are hard to justify. To the extent of our knowledge, no previous work on U-OOD detection had provided a similar theoretical tool capable of interpreting and explaining results.

5 Conclusion

Our work explores the state of U-OOD detection by observing the behavior of methods on an extensive and varied set of tasks. By doing so, we show a complicated landscape, with most methods being highly inconsistent among and within tasks. **MahaAD** is however an exception to this trend, behaving consistently in a large majority of experimental configurations. Consequently, **MahaAD** appears to be the current best off-the-shelf unsupervised OOD detector, as it offers good performance and consistency without requiring time-consuming data pre-processing, careful tuning of the training procedure, or hyperparameter search.

In order to explain these inconsistent results, we introduced a characterization of U-OOD based on training set invariants and showed that the **MahaAD** method embodies a linear version of this concept. We found this framework useful to not only qualitatively understand U-OOD detector predictions, but also to assess whether a test dataset is in fact OOD or not. A key take-away is that we cannot purely rely on semantic labels from datasets to design U-OOD evaluation methods, as done in previous works.

In general, this points to a rather bleak conclusion: at the moment, no method can consistently outperform a simple anomaly detector that uses naively extracted features from a network trained on a different dataset and which was optimized for a different task. We believe that with our invariant-based U-OOD characterization, new appropriate methods can be designed and validated in comprehensive ways.

References

- [1] Davide Abati et al. "Latent space autoregression for novelty detection". In: *Proceedings of the IEEE/CVF Conference on Computer Vision and Pattern Recognition*. 2019, pp. 481–490.
- [2] Faruk Ahmed and Aaron Courville. "Detecting semantic anomalies". In: *Proceedings of the AAAI Conference on Artificial Intelligence*. Vol. 34. 2020, pp. 3154–3162.
- [3] Samet Akcay, Amir Atapour-Abarghouei, and Toby P Breckon. "Ganomaly: Semi-supervised anomaly detection via adversarial training". In: *Asian conference on computer vision*. Springer. 2018, pp. 622–637.

- [4] Dario Amodei et al. “Concrete problems in AI safety”. In: *arXiv preprint arXiv:1606.06565* (2016).
- [5] Muhammad S Battikh and Artem A Lenskiy. “Latent-Insensitive Autoencoders for Anomaly Detection and Class-Incremental Learning”. In: *arXiv preprint arXiv:2110.13101* (2021).
- [6] Liron Bergman, Niv Cohen, and Yedid Hoshen. “Deep nearest neighbor anomaly detection”. In: *arXiv preprint arXiv:2002.10445* (2020).
- [7] Liron Bergman and Yedid Hoshen. “Classification-based anomaly detection for general data”. In: *arXiv preprint arXiv:2005.02359* (2020).
- [8] Paul Bergmann et al. “Improving unsupervised defect segmentation by applying structural similarity to autoencoders”. In: *arXiv preprint arXiv:1807.02011* (2018).
- [9] Paul Bergmann et al. “MVTec AD – A Comprehensive Real-World Dataset for Unsupervised Anomaly Detection”. In: *Proceedings of the IEEE/CVF Conference on Computer Vision and Pattern Recognition (CVPR)*. June 2019.
- [10] Paul Bergmann et al. “Uninformed students: Student-teacher anomaly detection with discriminative latent embeddings”. In: *Proceedings of the IEEE/CVF Conference on Computer Vision and Pattern Recognition*. 2020, pp. 4183–4192.
- [11] Behzad Bozorgtabar et al. “SALAD: Self-supervised Aggregation Learning for Anomaly Detection on X-Rays”. In: *International Conference on Medical Image Computing and Computer-Assisted Intervention*. Springer. 2020, pp. 468–478.
- [12] Markus M Breunig et al. “LOF: identifying density-based local outliers”. In: *Proceedings of the 2000 ACM SIGMOD international conference on Management of data*. 2000, pp. 93–104.
- [13] Raghavendra Chalapathy and Sanjay Chawla. “Deep learning for anomaly detection: A survey”. In: *arXiv preprint arXiv:1901.03407* (2019).
- [14] Raghavendra Chalapathy, Aditya Krishna Menon, and Sanjay Chawla. “Anomaly detection using one-class neural networks”. In: *arXiv preprint arXiv:1802.06360* (2018).
- [15] Hyunsun Choi, Eric Jang, and Alexander A Alemi. “Waic, but why? generative ensembles for robust anomaly detection”. In: *arXiv preprint arXiv:1810.01392* (2018).
- [16] Sungik Choi and Sae-Young Chung. “Novelty detection via blurring”. In: *arXiv preprint arXiv:1911.11943* (2019).
- [17] Niv Cohen and Yedid Hoshen. “Sub-image anomaly detection with deep pyramid correspondences”. In: *arXiv preprint arXiv:2005.02357* (2020).
- [18] Anne-Sophie Collin and Christophe De Vleeschouwer. “Improved anomaly detection by training an autoencoder with skip connections on images corrupted with Stain-shaped noise”. In: *2020 25th International Conference on Pattern Recognition (ICPR)*. IEEE. 2021, pp. 7915–7922.
- [19] Thomas Defard et al. “PaDiM: a Patch Distribution Modeling Framework for Anomaly Detection and Localization”. In: *arXiv preprint arXiv:2011.08785* (2020).
- [20] David Dehaene et al. “Iterative energy-based projection on a normal data manifold for anomaly localization”. In: *arXiv preprint arXiv:2002.03734* (2020).
- [21] Yilun Du and Igor Mordatch. “Implicit generation and generalization in energy-based models”. In: *arXiv preprint arXiv:1903.08689* (2019).
- [22] Izhak Golan and Ran El-Yaniv. “Deep anomaly detection using geometric transformations”. In: *Advances in Neural Information Processing Systems*. 2018, pp. 9758–9769.
- [23] Dong Gong et al. “Memorizing normality to detect anomaly: Memory-augmented deep autoencoder for unsupervised anomaly detection”. In: *Proceedings of the IEEE/CVF International Conference on Computer Vision*. 2019, pp. 1705–1714.
- [24] Sachin Goyal et al. “DROCC: Deep robust one-class classification”. In: *International Conference on Machine Learning*. PMLR. 2020, pp. 3711–3721.
- [25] Ben Graham. “Kaggle diabetic retinopathy detection competition report”. In: *University of Warwick* (2015).
- [26] Jakob D Havtorn et al. “Hierarchical VAEs Know What They Don’t Know”. In: *arXiv preprint arXiv:2102.08248* (2021).
- [27] Dan Hendrycks and Kevin Gimpel. “A baseline for detecting misclassified and out-of-distribution examples in neural networks”. In: *arXiv preprint arXiv:1610.02136* (2016).

- [28] Dan Hendrycks et al. “Using self-supervised learning can improve model robustness and uncertainty”. In: *arXiv preprint arXiv:1906.12340* (2019).
- [29] R Devon Hjelm et al. “Learning deep representations by mutual information estimation and maximization”. In: *arXiv preprint arXiv:1808.06670* (2018).
- [30] Jinlei Hou et al. “Divide-and-Assemble: Learning Block-wise Memory for Unsupervised Anomaly Detection”. In: *arXiv preprint arXiv:2107.13118* (2021).
- [31] Yen-Chang Hsu et al. “Generalized odin: Detecting out-of-distribution image without learning from out-of-distribution data”. In: *Proceedings of the IEEE/CVF Conference on Computer Vision and Pattern Recognition*. 2020, pp. 10951–10960.
- [32] Chaoqin Huang et al. “Attribute restoration framework for anomaly detection”. In: *arXiv preprint arXiv:1911.10676* (2019).
- [33] Xu Ji, Joao F Henriques, and Andrea Vedaldi. “Invariant information distillation for unsupervised image segmentation and clustering”. In: *arXiv preprint arXiv:1807.06653* 2.3 (2018), p. 8.
- [34] Ryo Kamoi and Kei Kobayashi. “Why is the Mahalanobis Distance Effective for Anomaly Detection?” In: *arXiv preprint arXiv:2003.00402* (2020).
- [35] Diederik P Kingma and Prafulla Dhariwal. “Glow: Generative flow with invertible 1x1 convolutions”. In: *arXiv preprint arXiv:1807.03039* (2018).
- [36] Rajat Koner et al. “OODformer: Out-Of-Distribution Detection Transformer”. In: *arXiv preprint arXiv:2107.08976* (2021).
- [37] Alex Krizhevsky, Geoffrey Hinton, et al. “Learning multiple layers of features from tiny images”. In: (2009).
- [38] Chun-Liang Li et al. “CutPaste: Self-Supervised Learning for Anomaly Detection and Localization”. In: *Proceedings of the IEEE/CVF Conference on Computer Vision and Pattern Recognition*. 2021, pp. 9664–9674.
- [39] Xiaoyan Li et al. “Exploring deep anomaly detection methods based on capsule net”. In: *arXiv preprint arXiv:1907.06312* (2019).
- [40] Fei Tony Liu, Kai Ming Ting, and Zhi-Hua Zhou. “Isolation forest”. In: *2008 eighth IEEE international conference on data mining*. IEEE. 2008, pp. 413–422.
- [41] Pablo Márquez-Neila and Raphael Sznitman. “Image Data Validation for Medical Systems”. In: *International Conference on Medical Image Computing and Computer-Assisted Intervention*. Springer. 2019, pp. 329–337.
- [42] Michael Mesarcik et al. “Improving Novelty Detection using the Reconstructions of Nearest Neighbours”. In: *arXiv preprint arXiv:2111.06150* (2021).
- [43] Sina Mohseni, Arash Vahdat, and Jay Yadawa. “Multi-task Transformation Learning for Robust Out-of-Distribution Detection”. In: *arXiv preprint arXiv:2106.03899* (2021).
- [44] Warren R Morningstar et al. “Density of states estimation for out-of-distribution detection”. In: *arXiv preprint arXiv:2006.09273* (2020).
- [45] Eric Nalisnick et al. “Detecting out-of-distribution inputs to deep generative models using a test for typicality”. In: *arXiv preprint arXiv:1906.02994* 5 (2019), p. 5.
- [46] Eric Nalisnick et al. “Do deep generative models know what they don’t know?” In: *arXiv preprint arXiv:1810.09136* (2018).
- [47] Yuval Netzer et al. “Reading digits in natural images with unsupervised feature learning”. In: (2011).
- [48] Khalil Ouardini et al. “Towards practical unsupervised anomaly detection on retinal images”. In: *Domain Adaptation and Representation Transfer and Medical Image Learning with Less Labels and Imperfect Data*. Springer, 2019, pp. 225–234.
- [49] Guansong Pang et al. “Deep learning for anomaly detection: A review”. In: *ACM Computing Surveys (CSUR)* 54.2 (2021), pp. 1–38.
- [50] Xingchao Peng et al. “Moment matching for multi-source domain adaptation”. In: *Proceedings of the IEEE/CVF International Conference on Computer Vision*. 2019, pp. 1406–1415.
- [51] Pramuditha Perera, Ramesh Nallapati, and Bing Xiang. “Ocgan: One-class novelty detection using gans with constrained latent representations”. In: *Proceedings of the IEEE/CVF Conference on Computer Vision and Pattern Recognition*. 2019, pp. 2898–2906.

- [52] Pramuditha Perera, Poojan Oza, and Vishal M Patel. “One-Class Classification: A Survey”. In: *arXiv preprint arXiv:2101.03064* (2021).
- [53] Alexander Podolskiy et al. “Revisiting Mahalanobis Distance for Transformer-Based Out-of-Domain Detection”. In: *arXiv preprint arXiv:2101.03778* (2021).
- [54] Tal Reiss and Yedid Hoshen. “Mean-Shifted Contrastive Loss for Anomaly Detection”. In: *arXiv preprint arXiv:2106.03844* (2021).
- [55] Tal Reiss et al. “PANDA: Adapting Pretrained Features for Anomaly Detection and Segmentation”. In: *Proceedings of the IEEE/CVF Conference on Computer Vision and Pattern Recognition*. 2021, pp. 2806–2814.
- [56] Jie Ren et al. “Likelihood ratios for out-of-distribution detection”. In: *Advances in Neural Information Processing Systems*. 2019, pp. 14707–14718.
- [57] Oliver Rippel, Patrick Mertens, and Dorit Merhof. “Modeling the distribution of normal data in pre-trained deep features for anomaly detection”. In: *arXiv preprint arXiv:2005.14140* (2020).
- [58] Lukas Ruff et al. “A unifying review of deep and shallow anomaly detection”. In: *Proceedings of the IEEE* (2021).
- [59] Lukas Ruff et al. “Deep one-class classification”. In: *International conference on machine learning*. PMLR. 2018, pp. 4393–4402.
- [60] Mohammad Sabokrou et al. “Avid: Adversarial visual irregularity detection”. In: *Asian Conference on Computer Vision*. Springer. 2018, pp. 488–505.
- [61] Mayu Sakurada and Takehisa Yairi. “Anomaly detection using autoencoders with nonlinear dimensionality reduction”. In: *Proceedings of the MLSDA 2014 2nd Workshop on Machine Learning for Sensory Data Analysis*. 2014, pp. 4–11.
- [62] Mohammadreza Salehi et al. “Arae: Adversarially robust training of autoencoders improves novelty detection”. In: *arXiv preprint arXiv:2003.05669* (2020).
- [63] Mohammadreza Salehi et al. “Multiresolution knowledge distillation for anomaly detection”. In: *Proceedings of the IEEE/CVF Conference on Computer Vision and Pattern Recognition*. 2021, pp. 14902–14912.
- [64] Mohammadreza Salehi et al. “Puzzle-AE: Novelty detection in images through solving puzzles”. In: *arXiv preprint arXiv:2008.12959* (2020).
- [65] Tim Salimans et al. “Pixelcnn++: Improving the pixelcnn with discretized logistic mixture likelihood and other modifications”. In: *arXiv preprint arXiv:1701.05517* (2017).
- [66] Robin Tibor Schirrmester et al. “Understanding anomaly detection with deep invertible networks through hierarchies of distributions and features”. In: *arXiv preprint arXiv:2006.10848* (2020).
- [67] Thomas Schlegl et al. “Unsupervised anomaly detection with generative adversarial networks to guide marker discovery”. In: *International conference on information processing in medical imaging*. Springer. 2017, pp. 146–157.
- [68] Bernhard Schölkopf et al. “Support vector method for novelty detection.” In: *NIPS*. Vol. 12. Citeseer. 1999, pp. 582–588.
- [69] Vikash Sehwal, Mung Chiang, and Prateek Mittal. “Ssd: A unified framework for self-supervised outlier detection”. In: *arXiv preprint arXiv:2103.12051* (2021).
- [70] Joan Serra et al. “Input complexity and out-of-distribution detection with likelihood-based generative models”. In: *arXiv preprint arXiv:1909.11480* (2019).
- [71] Kihyuk Sohn et al. “Learning and evaluating representations for deep one-class classification”. In: *arXiv preprint arXiv:2011.02578* (2020).
- [72] Jihoon Tack et al. “Csi: Novelty detection via contrastive learning on distributionally shifted instances”. In: *arXiv preprint arXiv:2007.08176* (2020).
- [73] Yu-Xing Tang et al. “Abnormal chest X-ray identification with generative adversarial one-class classifier”. In: *2019 IEEE 16th International Symposium on Biomedical Imaging (ISBI 2019)*. IEEE. 2019, pp. 1358–1361.
- [74] Yu-Xing Tang et al. “Automated abnormality classification of chest radiographs using deep convolutional neural networks”. In: *NPJ digital medicine* 3.1 (2020), pp. 1–8.
- [75] Antonio Torralba, Rob Fergus, and William T Freeman. “80 million tiny images: A large data set for nonparametric object and scene recognition”. In: *IEEE transactions on pattern analysis and machine intelligence* 30.11 (2008), pp. 1958–1970.

- [76] Shashanka Venkataramanan et al. “Attention guided anomaly localization in images”. In: *European Conference on Computer Vision*. Springer. 2020, pp. 485–503.
- [77] Siqi Wang et al. “Effective end-to-end unsupervised outlier detection via inlier priority of discriminative network”. In: *Advances in Neural Information Processing Systems*. 2019, pp. 5962–5975.
- [78] Xiaosong Wang et al. “Chestx-ray8: Hospital-scale chest x-ray database and benchmarks on weakly-supervised classification and localization of common thorax diseases”. In: *Proceedings of the IEEE conference on computer vision and pattern recognition*. 2017, pp. 2097–2106.
- [79] Zhisheng Xiao, Qing Yan, and Yali Amit. “Do We Really Need to Learn Representations from In-domain Data for Outlier Detection?” In: *arXiv preprint arXiv:2105.09270* (2021).
- [80] Zhisheng Xiao, Qing Yan, and Yali Amit. “Likelihood regret: An out-of-distribution detection score for variational auto-encoder”. In: *arXiv preprint arXiv:2003.02977* (2020).
- [81] Zhisheng Xiao et al. “VaeBM: A symbiosis between variational autoencoders and energy-based models”. In: *International Conference on Learning Representations*. 2020.
- [82] Sangwoong Yoon, Yung-Kyun Noh, and Frank Chongwoo Park. “Autoencoding Under Normalization Constraints”. In: *arXiv preprint arXiv:2105.05735* (2021).
- [83] Shuangfei Zhai et al. “Deep structured energy based models for anomaly detection”. In: *International Conference on Machine Learning*. PMLR. 2016, pp. 1100–1109.
- [84] Bo Zong et al. “Deep autoencoding gaussian mixture model for unsupervised anomaly detection”. In: *International conference on learning representations*. 2018.

6 Supplementary Material

6.1 Dataset Details

We briefly describe all datasets used in our experiments. An overview of our experimental set-up is given in Table 2.

CIFAR10 [37]. (In) small, natural images divided into 10 classes. For *uni-class*, one class forms the in-distribution, with its test set used in the evaluation. For *shift-low-res*, all 50000 training images are used for training when considered in-distribution, and all 10000 test images are used for testing. (Out) The remaining 9 classes are used as OOD for *uni-class*, subsampled to 1000 images.

CIFAR100 [37]. (In) 20 experiments with the training set of one of the semantic superclasses as the in-distribution, with its test set used during evaluation. (Out) Images from the remaining superclasses, subsampled to 500 images. Also used as an OOD dataset with CIFAR10 as in.

SVHN [47]. A dataset consisting of images of house numbers. We only use it as an OOD dataset, where the test set is reduced to 10000 samples.

DomainNet [50]. (In) The train and test images from the first 173 classes are used for training and evaluation respectively (as in [31]). We perform 11 experiments with the real images, and 11 with infographs. (Out) The remaining 11 domain-class combinations are used as OOD datasets. All test sets are downsampled to 5000 images.

MVTec [9]. (In) Between 60 and 391 aligned images of 15 different objects and textures. 12-60 images are used as the in-distribution at test time. (Out) 30-141 images of defect objects are used as OOD.

OCT. (In) A collection of 58849 retinal Optical Coherence Tomography images used for training, and 300 for testing. (Out) Corrupted OCT scans built as described in [41].

Chest [78]. (In) The NIH Clinical Center ChestX-ray dataset containing 85524 training images. We use 300 images from the test set during evaluation. (Out) Corrupted X-ray scans as described in [41].

NIH [74]. (In) A collection of 4261 healthy X-ray scans of the NIH Clinical Center ChestX-ray dataset. The healthy test scans are used as the in-distribution during evaluation. (Out) Pathological scans from the same dataset.

DRD [25]. (In) 25809 healthy high-resolution retinal fundus photographs. Healthy test scans are again used during evaluation. (Out) Retinal fundus photographs depicting 4 different levels of diabetic retinopathy (DR). The level of DR is indicated by a digit next to the method’s name (DRD1–DRD4).

6.2 Implementation Details

We provide a short description of all models compared and their implementations.

MSCL [54] uses a novel contrastive loss function to fine-tune the final two blocks of a pretrained network, and combines this with an angular center loss for a final score. We used the official implementation with the learning rate set to $5 \cdot 10^{-5}$, as described in the paper, and trained until convergence.

SSD₃₂ [69] uses contrastive learning for self-supervised representation learning. Then, it scores samples by the Mahalanobis distance. computed at the last layer. All images were resized to 32×32 and processed with a ResNet-101.

SSD₂₂₄ is equivalent to SSD₃₂ but resizing high-resolution images to 224×224 instead. We lowered the batch size to 12 and use a ResNet-50 to deal with memory limitations. This method was not applied over datasets with small resolution images.

MKD [63] learns a cloner network to imitate the activations of a source network at multiple layers and scores samples by the discrepancy between the predictions of the two. We trained until convergence and used the default settings from the original work.

Category	# Tasks	Tasks	# train	# in	# out
<i>uni-class</i>	10	{airplane,automobile,bird,cat,deer, dog,frog,horse,ship,truck}:rest	5000	1000	1000
<i>uni-super</i>	20	{aquatic mammals,fish,flowers,food containers,fruit and vegetables, household electrical devices,household furniture,insects, large carnivores,large man-made outdoor things, large natural outdoor scenes,large omnivores and herbivores, medium-sized mammals,non-insect invertebrates, people,reptiles,small mammals,trees,vehicles 1,vehicles 2}:rest	2500	500	500
<i>uni-ano</i>	15	{bottle,cable,capsule,carpet,grid,hazelnut, leather,metal nut,pill,screw,tile, toothbrush,transistor,wood,zipper}:defect	60-391	12-60	30-141
<i>uni-med</i>	1	OCT:corruptions	58849	300	300
	1	Chest:corruptions	85524	300	300
	1	NIH:pathology	4261	677	667
	4	DRD:DRD1-4	25809	500	500
<i>shift-low-res</i>	2	CIFAR10:{SVHN,CIFAR100}	50000	10000	10000
<i>shift-high-res</i>	11	Real A:{Quickdraw A,Quickdraw B,Infograph A, Infograph B,Sketch A,Sketch B,Real B, Clipart A,Clipart B,Painting A,Painting B}	61817	5000	5000
	11	Infograph A:{Quickdraw A,Quickdraw B, Sketch A,Sketch B,Real A,Real B, Clipart A,Clipart B,Painting A,Painting B}	14069	5000	5000

Table 2: Experimental set-up.

DDV [41] aims to build an efficient latent representation by iteratively maximizing the log-likelihood of the low-dimensional latent vectors of the training images, computed with a ResNet-50. Anomaly scores are given by the negative log-likelihood. We use our own implementation of DDV, following the settings described in its paper, i.e., a latent space of dimensionality 16 and a bandwidth of 10^{-2} [41].

DN2 [6] scores outliers by computing the mean distance to its 2 nearest neighbour on features extracted from the penultimate layer of a ResNet-152 pre-trained on ImageNet.

MHRot [28] trains a multi-headed classifier to predict the correct transformation applied to an image. At test time, the classifier’s softmax scores are combined for a final OOD score. Models are trained with the default settings until convergence of the validation loss. We use a ResNet-101 instead of a ResNet-18.

Glow [35] is a generative flow-based model, that allows for the exact computation of the likelihood, which we use as the anomaly score at test time. We use an architecture with three blocks of 32 layers each. Images are resized to 32×32 .

IC [70] aims to correct the high likelihood that generative models tend to assign to simple inputs, such as constant color images. To this end, IC computes the ratio between the likelihood of the generative model and a complexity score of the input image. We used Glow as our generative model and the length of the PNG image encoding as the complexity estimate.

HierAD [66] computes the ratio between the Glow generative model likelihood and a general background likelihood consisting of a Glow model trained on the *80 Million Tiny Images* dataset [75]. To make the method fully unsupervised, we do not use their proposed outlier loss during training.

MahaAD [57] is the Mahalanobis anomaly detector. We use a ResNet-101, ResNet-152 and an EfficientNet-b4 as described in [57]. With the ResNets, we resize images to 224×224 , while for the EfficientNet-b4 this is 380×380 .

Unless stated otherwise, all input images are rescaled to 224×224 .

	Airplane	Automobile	Bird	Cat	Deer	Dog	Frog	Horse	Ship	Truck	Average	FP
OCSVM [68]	63.0	44.0	64.9	48.7	73.5	50.0	72.5	53.3	64.9	50.8	58.5	Dec 1999
AnoGAN [67]	67.1	54.7	52.9	54.5	65.1	60.3	58.5	62.5	75.8	66.5	61.8	Mar 2017
RCAE [14]	72.0	63.1	71.7	60.6	72.8	64.0	64.9	63.6	74.7	74.5	68.2	Feb 2018
GT [22]	74.7	95.7	78.1	72.4	87.8	87.8	83.4	95.5	93.3	91.3	86.0	May 2018
Glow* [35]	76.1	44.5	60.3	57.3	43.9	55.1	36.2	46.4	71.0	46.4	53.7	Jul 2018
LSA [1]	73.5	58.0	69.0	54.2	76.1	54.6	75.1	53.5	71.7	54.8	64.1	Jul 2018
DSVDD [59]	61.7	65.9	50.8	59.1	60.9	65.7	67.7	67.3	75.9	73.1	64.8	Jul 2018
IIC [33]	68.4	89.4	49.8	65.3	60.5	59.1	49.3	74.8	81.8	75.7	67.4	Jul 2018
DIM [29]	72.6	52.3	60.5	53.9	66.7	51.0	62.7	59.2	52.8	47.6	57.9	Aug 2018
OCGAN [51]	75.7	53.1	64.0	62.0	72.3	62.0	72.3	57.5	82.0	55.4	65.6	Mar 2019
MHRot [28]	77.5	96.9	87.3	80.9	92.7	90.2	90.9	96.5	95.2	93.3	90.1	Jun 2019
CapsNet [39]	62.2	45.5	67.1	67.5	68.3	63.5	72.7	67.3	71.0	46.6	61.2	Jul 2019
IC* [70]	38.3	62.0	45.5	61.5	48.7	63.9	62.6	63.7	48.4	58.8	55.3	Jul 2019
E3Outlier [77]	79.4	95.3	75.4	73.9	84.1	87.9	85.0	93.4	92.3	89.7	85.6	Sep 2019
DDV* [41]	67.0	58.0	55.9	56.9	60.9	57.3	56.8	55.4	65.0	64.6	59.8	Oct 2019
DeepIF [48]	-	-	-	-	-	-	-	-	-	-	88.2	Oct 2019
CAVGA-DU [76]	65.3	78.4	76.1	74.7	77.5	55.2	81.3	74.5	80.1	74.1	73.7	Nov 2019
U-Std [10]	78.9	84.9	73.4	74.8	85.1	79.3	89.2	83.0	86.2	84.8	82.0	Nov 2019
InvAE [32]	78.5	89.8	86.1	77.4	90.5	84.5	89.2	92.9	92.0	85.5	86.6	Nov 2019
DROCC [24]	81.7	76.7	66.7	67.1	73.6	74.4	74.4	71.4	80.0	76.2	74.2	Feb 2020
DN2 [6]	93.9	97.7	85.5	83.6	91.3	94.3	93.6	95.1	95.3	93.3	92.5	Feb 2020
ARAE [62]	72.2	43.1	69.0	55.0	75.2	54.7	70.1	51.0	72.2	40.0	60.2	Mar 2020
GOAD [7]	77.2	96.7	83.3	77.7	87.8	87.8	90.0	96.1	93.8	92.0	88.2	May 2020
MahaAD* _{RN101} [57]	92.9	96.4	85.8	85	93.8	91.1	94.1	94.8	95.4	96.8	92.6	May 2020
MahaAD* _{RN152} [57]	93.8	96.4	87.6	85.3	94.5	91.2	95	95.2	95.5	96.4	93.1	May 2020
MahaAD* _{ENB4} [57]	95.1	97.8	92.3	91.6	96.5	96.8	97.6	96.9	97.4	98.3	96.0	May 2020
HierAD* [66]	47.6	63.4	63.2	59.0	79.2	64.3	77.5	66.4	61.6	59.8	64.2	Jun 2020
CSI [72]	89.9	99.9	93.1	86.4	93.9	93.2	95.1	98.7	97.9	95.5	94.3	Jul 2020
Puzzle-AE [64]	78.9	78.1	70.0	54.9	75.5	66.0	74.8	73.3	83.3	70.0	72.5	Aug 2020
PANDA [55]	97.4	98.4	93.9	90.6	97.5	94.4	97.5	97.5	97.6	97.4	96.2	Oct 2020
ConDA [71]	90.9	98.9	88.1	83.1	89.9	90.3	93.5	98.2	96.5	95.2	92.5	Nov 2020
MKD [63]	90.5	90.4	79.7	77.0	86.7	91.4	89.0	86.8	91.5	88.9	87.2	Nov 2020
SSD [69]	82.7	98.5	84.2	84.5	84.8	90.9	91.7	95.2	92.9	94.4	90.0	Mar 2021
SSL [79]	94.8	96.4	88.3	87.6	92.7	94.2	96.4	94.3	96.1	97.0	93.8	May 2021
MTL [43]	84.3	96.0	87.7	82.3	91.0	91.5	91.1	96.3	96.3	92.3	90.9	Jun 2021
MSCL [54]	97.7	98.9	95.8	94.5	97.3	97.1	98.4	98.3	98.7	98.4	97.5	Jun 2021
OODformer [36]	92.3	99.4	95.6	93.1	94.1	92.9	96.2	99.1	98.6	95.8	95.7	Jul 2021
DaA [30]	-	-	-	-	-	-	-	-	-	-	75.3	Jul 2021

Table 3: AUC scores for *uni-class*. First published (FP) column contains the dates of first online appearance.

* Our results

	0	1	2	3	4	5	6	7	8	9	10	11	12	13	14	15	16	17	18	19	Mean
Glow* [35]	60.7	59.4	25.4	65.7	45.5	66.9	66.1	46.0	46.0	64.8	75.5	51.1	54.0	48.8	50.6	50.2	52.8	50.1	44.1	53.3	53.8
IC* [70]	61.2	53.9	44.4	44.4	48.3	46.4	41.9	51.2	72.0	58.0	48.7	68.3	69.8	51.6	56.1	62.0	62.4	68.8	59.5	48.8	55.9
OC-SVM [68]	68.4	63.6	52	64.7	58.2	54.9	57.2	62.9	65.6	74.1	84.1	58	68.5	64.6	51.2	62.8	66.6	73.7	52.8	58.4	63.1
DAGMM [84]	43.4	49.5	66.1	52.6	56.9	52.4	55	52.8	53.2	42.5	52.7	46.4	42.7	45.4	57.2	48.8	54.4	36.4	52.4	50.3	50.6
DSEBM [83]	64	47.9	53.7	48.4	59.7	46.6	51.7	54.8	66.7	71.2	78.3	62.7	66.8	52.6	44	56.8	63.1	73	57.7	55.5	58.8
DDV* [41]	67.3	67.0	61.2	48.9	75.6	48.6	58.3	60.0	60.9	60.0	71.6	59.0	56.4	53.6	58.0	56.2	58.3	67.6	57.7	62.4	60.4
HierAD* [66]	68.7	59.5	76.5	35.9	59.7	31.6	48.5	59.6	78.4	65.1	76.9	67.6	77.1	55.1	59.1	63.2	69.6	80.1	58.4	57.7	62.4
DVSDD [59]	66	60.1	59.2	58.7	60.9	54.2	63.7	66.1	74.8	78.3	80.4	68.3	75.6	61	64.3	66.3	72	75.9	67.4	65.8	67.0
GOAD [7]	73.9	69.2	67.6	71.8	72.7	67	80	59.1	79.5	83.7	84	68.7	75.1	56.6	83.8	66.9	67.5	91.6	88	82.6	74.5
MHRot [28]	77.6	72.8	71.9	81	81.1	66.7	87.9	69.4	86.8	91.7	87.3	85.4	85.1	60.3	92.7	70.4	78.3	93.5	89.6	88.1	80.1
SSD* [69]	76.5	79.6	88.7	73.4	91.1	72.4	73.9	79.8	80.7	86.0	72.3	79.4	83.1	74.5	87.3	74.4	79.9	90.9	83.3	80.7	80.4
ConDA [71]	82.9	84.3	88.6	86.4	92.6	84.5	73.4	84.2	87.7	94.1	85.2	87.8	82	82.7	93.4	75.8	80.3	97.5	94.4	92.4	86.5
CSI [72]	86.3	84.8	88.9	85.7	93.7	81.9	91.8	83.9	91.6	95	94	90.1	90.3	81.5	94.4	85.6	83	97.5	95.9	95.2	89.6
MKD* [63]	90.3	89.7	90.1	89.9	89.8	90.2	89.7	90.3	90.0	89.5	88.5	90.2	91.0	89.6	89.0	89.8	90.4	88.9	90.1	90.7	89.9
DN2* [6]	85.9	88.8	93.4	93.1	94.7	94.1	94.3	86.0	91.0	92.3	97.0	83.0	88.5	87.8	95.5	81.6	86.9	95.5	89.2	90.7	90.5
PANDA [55]	91.5	92.6	98.3	96.6	96.3	94.1	96.4	91.2	94.7	94	96.4	92.6	93.1	89.4	98	89.7	92.1	97.7	94.7	92.7	94.1
MSCL [54]	96.2	95.9	98.4	97.7	97.6	96.5	98.6	94.1	97.1	96.6	97.4	96.3	95.6	93.0	98.9	92.6	95.4	98.5	97.4	97.0	96.5
MahaAD* _{RN101} [57]	91.9	89.5	96	95.3	94.7	91.1	95.2	89.5	93.6	93.7	95.4	90.6	91.4	84.3	96.7	84.5	87.7	97.1	94.4	92.8	92.3
MahaAD* _{RN152} [57]	91.4	90.8	96.3	95.6	95.4	91.5	95.6	89.2	93.4	93.9	94.9	90.3	91.2	85.5	97.1	85.9	89	97.1	94.5	92.6	92.6
MahaAD* _{ENB4} [57]	93.2	92.8	96.7	97.8	97.2	95.4	98.0	92.6	95.9	94.9	95.8	93.0	93.0	89.2	97.8	89.1	91.7	97.5	96.2	94.8	94.6

Table 4: AUC scores for *uni-super*.

6.3 Extended results

In Table 3 to Table 9 we dissect the per-task results from Table 1, reporting the AUC scores for each individual experiment and including some additional methods that were omitted from the main text for clarity.

	CIFAR10:SVHN	CIFAR10:CIFAR100
Glow [66]	8.8	51.7
DSVDD [59]	14.5	52.1
MKD* [63]	26.8	66.2
DDV* [41]	57.9	54.2
EBM [21]	63.0	50.0
DN2* [6]	74.5	79.2
VAEBM [81]	83.0	62.0
MSCL* [54]	83.7	78.3
TT [45]	87.0	54.8
LLRe [80]	87.5	
BIVA [26]	89.1	
NAE [82]	92.0	
HierAD [66]	93.9	66.8
IC [70]	95.0	73.6
GOAD [7]	96.3	77.2
SVD-RND [16]	96.4	
MHRot [28]	97.8	82.3
DoSE [44]	97.3	56.9
CSI [72]	99.8	89.2
SSD [69]	99.6	90.6
MTL [43]	99.9	93.2
WAIC [44]	14.3	53.2
WAIC [15]	100	
MahaAD* _{RN101} [57]	94.3	74
MahaAD* _{RN152} [57]	96.6	76.6
MahaAD* _{ENB4} [57]	96.2	79.1

Table 5: AUC scores for *shift-low-res*.
* Our results

	QDa	QDb	IGa	IGb	SKa	SKb	REb	CAa	CAb	PNa	PNb	Mean
MSCL* [54]	78.8	78.6	84.0	85.6	79.9	82.7	70.2	76.9	81.8	73.9	81.6	79.5
SSD* [69]	40.3	40.4	69.0	69.6	68.9	73.9	68.6	53.1	58.8	77.6	83.3	64.0
MKD* [63]	24.2	23.1	56.6	52.7	47.2	47.3	52.8	49.4	47.3	68.6	70.4	48.9
DDV* [41]	75.3	88.4	62.1	54.3	72.1	58.3	50.2	64.4	58.4	51.4	63.9	63.5
DN2* [6]	43.8	45.0	76.5	74.3	67.6	72.6	72.6	68.7	73.4	78.8	84.3	68.9
MHRot* [28]	71.6	71.6	48.7	50.1	63.8	64.4	52.3	60.2	61.5	55.4	57.0	59.7
Glow* [35]	3.2	3.0	54.8	51.0	19.5	20.9	49.5	37.1	33.4	66.6	67.0	36.9
IC* [70]	89.9	90.4	66.4	68.8	69.5	68.8	52.0	64.4	66.3	55.9	55.7	68.0
HierAD* [66]	95.5	95.7	36.6	40.6	84.9	82.7	51.4	51.5	58.3	41.6	41.6	61.8
MahaAD* _{RN101} [57]	72.9	71.3	81.6	80.8	64.2	65.5	57.2	70.3	70	66	69.2	69.9
MahaAD* _{RN152} [57]	74.1	73.7	81.1	80.3	65.3	66.5	57.9	70.5	70.8	65.4	68.9	70.4
MahaAD* _{ENB4} [57]	79.7	80.4	76.3	76.9	73.8	76.3	67.7	71.0	73.5	70.5	77.5	74.9

Table 6: AUC scores for *shift-high-res* using Real-A as the in-distribution. QD: quickdraw, IG: infograph, SK: sketch, RE: real. A is the set without semantic shift, and B with semantic shift.
* Our results

	QDa	QDb	IGb	SKa	SKb	REa	REb	CAa	CAb	PNa	PNb	Mean
MSCL* [54]	50.4	50.0	58.8	76.9	78.7	76.6	80.8	75.0	74.7	78.9	80.2	71.0
SSD* [69]	35.1	33.5	56.3	67.9	69.1	56.7	57.7	69.4	69.3	57.3	58.5	57.3
MKD* [63]	83.0	82.4	48.0	81.7	80.4	88.9	91.0	84.5	82.5	95.6	95.2	83.0
DDV* [41]	76.9	77.7	50.0	51.8	54.4	57.5	62.0	58.7	58.5	61.1	62.5	61.0
DN2* [6]	58.4	60.1	53.5	73.1	75.0	82.5	88.7	77.5	77.3	90.0	91.3	75.2
MHRot* [28]	94.9	95.2	53.9	88.5	88.7	87.6	87.9	89.3	89.7	88.6	89.4	86.7
Glow* [35]	0.7	0.6	45.6	12.3	14.0	50.7	49.9	35.3	30.6	69.2	69.5	34.4
IC* [70]	94.1	94.4	54.0	64.8	63.5	42.9	44.8	60.3	62.4	46.7	46.8	61.3
HierAD* [66]	99.8	99.8	53.7	93.8	92.7	83.1	83.3	80.8	83.1	77.6	77.6	84.1
MahaAD* _{RN101} [57]	92.3	92.1	51.8	78.1	77.6	88.1	88.4	81.5	80.3	90.9	91.2	82.9
MahaAD* _{RN152} [57]	92.8	93.0	51.7	79.7	78.9	89.4	89.8	82.1	81.2	91.1	91.4	83.7
MahaAD* _{ENB4} [57]	94.5	94.8	52.3	89.5	89.0	93.6	94.7	87.4	87.1	94.9	95.4	88.5

Table 7: AUC scores for *shift-high-res* using Infograph-A as the in-distribution.
* Our results

	Carpet	Grid	Leather	Tile	Wood	Bottle	Cable	Capsule	HN	MN	Pill	Screw	TB	TS	Zipper	Mean
AVID [60]	70	59	58	66	83	88	64	85	86	63	86	66	73	58	84	73
AESSIM [8]	67	69	46	52	83	88	61	61	54	54	60	51	74	52	80	63
AEL2 [8]	50	78	44	77	74	80	56	62	88	73	62	69	98	71	80	71
AnoGAN [67]	49	51	52	51	68	69	53	58	50	50	62	35	57	67	59	55
LSA [11]	74	54	70	70	75	86	61	71	80	67	85	75	89	50	88	73
CAVGA-DU [76]	73	75	71	70	85	89	63	83	84	67	88	77	91	73	87	78
DSVDD [59]	54	59	73	81	87	86	71	69	71	75	77	64	70	65	74	72
VAE-grad [20]	67	83	71	81	89	86	56	86	74	78	80	71	89	70	67	77
GT [22]	46	61.9	82.5	53.9	48.2	74.3	84.8	67.8	33.3	82.4	65.2	44.6	94	79.8	87.4	67.1
Puzzle-AE [64]	65.7	75.4	72.9	65.5	89.5	94.2	87.9	66.9	91.2	66.3	71.6	57.8	97.8	86	75.7	77.6
MKD [63]	79.3	78	95.1	91.6	94.3	99.4	89.2	80.5	98.4	73.6	82.7	83.3	92.2	85.6	93.2	87.7
MSCL [54]	-	-	-	-	-	-	-	-	-	-	-	-	-	-	-	87.2
SSD* [69]	53.4	33.5	61.4	61.9	44.9	78.3	62.7	60.2	62.2	69.4	76.6	59.5	99.8	88.5	74.8	65.8
DDV* [41]	70.2	59.9	64.0	70.2	74.5	95.3	70.6	61.6	73.5	83.0	65	51.0	75.8	80.7	62.7	70.5
DN2* [6]	91	60.4	99.2	99.1	94	98	89.5	85.9	97.5	84.1	73.8	71.4	90.3	92.2	93.5	88
MHRot* [28]	47.8	58.9	75	51.2	90.2	82	79.9	59	73.6	75.7	64.9	36.6	86.9	86.5	93.4	70.8
Glow* [35]	72.9	98.3	94.1	83.7	96.9	96.6	83.3	67.1	90.5	62.4	84.8	31.8	87.6	88.4	91.3	82.0
IC* [70]	69.7	75.6	94.3	71.2	78.1	96.0	85.8	63.3	64.9	77.0	67.9	29.7	85.8	89.5	54.9	73.6
HierAD* [66]	73.4	95.3	95.5	84.5	97.5	97.3	86.5	70.0	75.0	73.6	74.2	26.2	98.6	92.5	84.1	81.6
SPADE [17]	-	-	-	-	-	-	-	-	-	-	-	-	-	-	-	85.5
FAVAE [20]	67.1	97	67.5	80.5	94.8	99.9	95	80.4	99.3	85.2	82.1	83.7	95.8	93.2	97.2	87.9
AEsc [18]	89	97	89	99	95	98	89	74	94	73	84	74	100	91	94	89
DaA [30]	86.6	95.7	86.2	88.2	98.2	97.6	84.4	76.7	92.1	75.8	90	98.7	99.2	87.6	85.9	89.5
MahaAD* _{RN101} [57]	79.5	59.6	99.3	100	98.2	99.3	91.6	93.8	99.4	93.4	90.6	72.1	98.6	96.1	97.9	91.3
MahaAD* _{RN152} [57]	78.3	64.7	98.6	99.8	98	99.6	95	95.4	100	91.9	89.4	74.9	97.8	96.8	97.5	91.8
MahaAD* _{ENB4} [57]	98.6	78.8	99.7	100	96.1	99.8	93.5	97.0	99.0	93.9	90.3	78.6	96.7	96.5	97.7	94.4

Table 8: AUC scores for *uni-ano*. HN is hazelnut, MN is metal nut, TB is toothbrush and TS is transistor.

	OCT	Chest	NIH	DRD1	DRD2	DRD3	DRD4
IF [40]							44.0
AnoGAN [67]							44.2
DSEBM [83]							43.1
DAGMM [84]							52.0
Glow [35]	44.8	54.6					
GT [7]			79.2				
DSVDD [59]	77.4	66.6	81.8				46.4
DeepIF [48]							74.5
DDV [41]	96.3	82.4	69.7*	59.8*	53.3*	44.0*	62.3*
GAOCC [73]			83.4				
MemDAE [11]			87.8				
MSCL* [54]	94.4	92.7	86.4	52.2	53.2	55.8	66.2
SSD* [69]	59.4	94.5	74.2	47.5	50.6	54.8	71.4
MKD* [63]	94.9	95.8	88.0	53.7	54.6	60.7	75.5
DN2* [6]	94.1	97.4	85.7	50.1	55.4	66.9	82.5
MHRot* [28]	87.7	96.2	81.8	49.0	50.2	52.7	65.3
Glow* [35]	62.3	49.8	65.0	52.2	47.5	54.7	59.5
IC* [70]	83.4	91.6	56.7	47.5	52.1	58.2	66.2
HierAD* [66]	94.3	99.0	79.8	52.1	51.7	57.5	73.5
MahaAD* _{RN101} [57]	98	99.8	84.6	52.1	52	63.6	79.9
MahaAD* _{RN152} [57]	97.6	99.8	86.5	51.2	51.2	61.8	78.8
MahaAD* _{ENB4} [57]	98.7	99.8	84.2	49.9	55.0	66.3	81.3

Table 9: AUC scores for *uni-med*.

* Our results